

Space Weather®








RESEARCH ARTICLE

10.1029/2022SW003152

Tong Dang and Xiaolei Li contributed equally to this work.

Unveiling the Space Weather During the Starlink Satellites Destruction Event on 4 February 2022

Tong Dang^{1,2,3} , Xiaolei Li^{1,2,3} , Bingxian Luo^{4,5} , Ruoxi Li^{1,2,3}, Binzheng Zhang⁶ , Kevin Pham⁷ , Dexin Ren^{1,2,3} , Xuetao Chen^{1,2,3} , Jiuhou Lei^{1,2,3} , and Yuming Wang^{1,2,3} 

¹CAS Key Laboratory of Geospace Environment, School of Earth and Space Sciences, University of Science and Technology of China, Hefei, China, ²CAS Center for Excellence in Comparative Planetology, Hefei, China, ³Mengcheng National Geophysical Observatory, University of Science and Technology of China, Hefei, China, ⁴Center for Space Science and Applied Research, Chinese Academy of Sciences, Beijing, China, ⁵School of Astronomy and Space Science, University of Chinese Academy of Sciences, Beijing, China, ⁶Department of Earth Sciences, The University of Hong Kong, Pokfulam, China, ⁷High Altitude Observatory, National Center for Atmospheric Research, Boulder, CO, USA

Key Points:

- We reveal the space weather process during 3–4 February 2022 geomagnetic storms, from the Sun to the satellite orbiting atmosphere
- Two coronal mass ejections led to the unexpected complex sequential storms and enhanced global atmospheric density over 20% at 210 km
- This event calls for the urgent need of accurate space weather prediction and collaborations between industry and space weather community

Supporting Information:

Supporting Information may be found in the online version of this article.

Correspondence to:

J. Lei and Y. Wang,
leijh@ustc.edu.cn;
ymwang@ustc.edu.cn

Citation:

Dang, T., Li, X., Luo, B., Li, R., Zhang, B., Pham, K., et al. (2022). Unveiling the space weather during the Starlink satellites destruction event on 4 February 2022. *Space Weather*, 20, e2022SW003152. <https://doi.org/10.1029/2022SW003152>

Received 9 MAY 2022

Accepted 28 JUL 2022

Author Contributions:

Conceptualization: Jiuhou Lei, Yuming Wang

Formal analysis: Tong Dang, Xiaolei Li, Ruoxi Li

Investigation: Tong Dang, Xiaolei Li, Bingxian Luo, Dexin Ren, Xuetao Chen, Jiuhou Lei, Yuming Wang

Methodology: Tong Dang, Ruoxi Li

Resources: Bingxian Luo

Supervision: Jiuhou Lei, Yuming Wang

Validation: Bingxian Luo

Abstract On 4 February 2022, 38 Starlink satellites were destroyed by the geomagnetic storm, which brought significant financial, aerospace and public influences. In this letter, we reveal the space weather process during 3–4 February 2022 geomagnetic disturbances, from the Sun all the way to the satellite orbiting atmosphere. Initiated by an M1.0 class flare and the following coronal mass ejection (CME), a moderate geomagnetic storm was stimulated on 3rd February by the CME arrival at Earth. Subsequently, another moderate storm was triggered on 4th February by the passage of another CME. Model simulations driven by solar wind show that the first geomagnetic storm induced around 20% atmospheric density perturbations at 210 km altitude on 3rd February. The unexpected subsequent storm on 4th February led to a density enhancement of around 20%–30% at around 210 km. The resulting atmospheric drag can be even larger, since the regional density enhancement was over 60% and the satellite orbits were continuously decaying. This event brings forth the urgent requirements of better understanding and accurate prediction of the space weather as well as collaborations between industry and space weather community.

Plain Language Summary The operating satellites in low-Earth orbit give the rapid information transfer between the satellites and the Earth. At the same time, these satellites are continuously slowed down and affected by the dense atmosphere of the Earth, which is referred to as the atmospheric drag. This effect can be greater during space weather events such as geomagnetic storms. Over the past years, thousands of Starlink satellites have been deployed by the SpaceX company into low-Earth orbit. However, on 4th February, 38 Starlink satellites were destroyed before they were lifted to a higher Earth orbit, which brought an economic loss estimated to be several tens of millions of dollars. Geomagnetic indices indicated two successive geomagnetic storms, which could warm the upper atmosphere and increase the atmospheric drag. In this work, we provide a comprehensive review on the process of space weather during this event from the Sun all the way to the terrestrial atmosphere. We have illustrated the solar eruption, solar wind propagation, and atmospheric density enhancement, using both observed data and model simulations. This study calls for more accurate modeling and better understanding of space weather as well as collaborations between industry and space weather community.

1. Introduction

The understanding of the Earth's space environment has grown exponentially over the centuries since the step into space age (Jacchia, 1959). The so-called space weather, which describes the “weather” changes in solar-terrestrial connections, has shown broad influences in civilian life, commerce, and national security, including communication, navigation, electric grids and satellite operations (Anthea et al., 2021; Emmert, 2015; Malandraki & Crosby, 2018; McNamara, 1991; Montenbruck & Gill, 2000; Skone & Yousuf, 2007; Zhang et al., 2019). Due to the existence of Earth's upper atmosphere, a large number of satellites and space debris operating between 100 and 600 km altitude are significantly affected by space weather via atmospheric drag (Chen et al., 2012, 2014; Li & Lei, 2021a; Qian & Solomon, 2012). The ever-increasing amount of space objects thus calls forth the urgent requirements to accurately understand and predict the four-dimensional spatial-temporal variation of the upper atmosphere as well as the space weather system (Krauss et al., 2020).

© 2022. The Authors.

This is an open access article under the terms of the [Creative Commons Attribution License](https://creativecommons.org/licenses/by/4.0/), which permits use, distribution and reproduction in any medium, provided the original work is properly cited.

Visualization: Tong Dang, Xiaolei Li, Ruoxi Li, Binzheng Zhang
Writing – original draft: Tong Dang, Xiaolei Li
Writing – review & editing: Binzheng Zhang, Kevin Pham, Jiuhou Lei, Yuming Wang

At 18:13 UT on 3 February 2022, the Falcon 9 rocket launched 49 Starlink satellites of SpaceX to the low Earth orbit, with a perigee of around 210 km above the Earth. 38 Starlink satellites were destroyed before they were lifted to a higher Earth orbit, which led to an economic loss expected to be several tens of millions of dollars (Hapgood et al., 2022). The geomagnetic indices suggested that two successive geomagnetic storms, which could warm the upper atmosphere and increase the atmospheric drag (Emmert, 2015; Prölss, 2011; Qian & Solomon, 2012), were ongoing during the satellite launch and operation. To better understand the possible influence of consecutive geomagnetic storms on satellite orbital decay, in this study, we reveal the space weather process during this event from the source Sun, to the interplanetary solar wind propagation, and to the upper atmosphere, based on observations and numerical simulations.

2. Methods

2.1. Coronal Observation

We investigate all the Coronal Mass Ejections (CMEs) that may arrive at Earth observed by the Large Angle and Spectrometric Coronagraph (LASCO) C2/C3 (Brueckner et al., 1995) on board the Solar and Heliospheric Observatory (SOHO) and the Sun Earth Connection Coronal and Heliospheric Investigation (SECCHI) COR2 (Howard et al., 2008) on board the Ahead Solar Terrestrial Relations Observatory (STEREO-A or STA). Between Jan 30 and Feb 1 in 2022, the SOHO was near the first Lagrange point of the Sun-Earth system while the STA traveled on the Ecliptic plane at a heliocentric distance of 0.97 AU with the separation angle of 35° upstream of the Earth. SOHO/LASCO C2/C3 and STA/SECCHI COR2 have sun-centered circular field of view with half-angle of 1.6° (6 Rs) and 4° (15 Rs). The difference coronagraph images were generated to highlight the coronal transients, including CMEs, from background long-lived coronal streamers and spike-like noises. With the two coronagraphs of SOHO/LASCO C2/C3 and STA/SECCHI COR2 from two perspectives almost at the same time, we apply Graduated Cylindrical Shell (GCS) modeling (Thernisien, 2011), an extensively used flux-rope like CME model, to fit the manually identified CME front in the coronagraph images and derive the CME geometric parameters of the GCS model. Based on the CME front positions at different times, we may further infer the velocity (v) of the CME front by using linear-fitting. For the two CMEs of interest in this study, the derived parameters are summarized in Table 1.

2.2. Atmospheric Density From Swarm-C Satellite

Swarm satellites were launched on 22 November 2013 and operated by European Space Agency. Swarm-C flew at an initial altitude of 462 km, with an inclination angle of around 87.35°. In this study, the atmospheric density derived from the Swarm-C accelerometer was used, and the retrieval from accelerometer to neutral density can be found in Doornbos (2012) and Li and Lei (2021b).

2.3. TIEGCM Model

The National Center for Atmospheric Research Thermosphere Ionosphere Electrodynamics General Circulation Model (TIEGCM) is a three-dimensional, self-consistent, and physics-based model of the coupled ionosphere-thermosphere system (Richmond et al., 1992; Roble et al., 1988). It also solves the ionospheric electrodynamic associated with the neutral wind dynamo (Richmond, 1995). The convection pattern at high latitudes is specified by the Weimer empirical model (Weimer, 2005), which is driven by the realistic solar wind and interplanetary magnetic field (IMF). In this study, the TIEGCM has a horizontal resolution of $1.25^\circ \times 1.25^\circ$ in geographic longitude and latitude (Dang et al., 2021) and a vertical resolution of 1/4 scale height. This relatively high-resolution grid resolves the dynamic evolution of large and meso-scale structures in the ionosphere-thermosphere coupled system.

3. Results

At about 23:00 UT on Jan 29, an M1.0 class flare occurred in the solar active region numbered 12936. It was accompanied by a coronal mass ejection (CME) captured by the coronagraphs (Brueckner et al., 1995; Howard et al., 2008) onboard SOHO and the STEREO-A spacecraft from two perspectives (see the inset of Figure 1) on the beginning of Jan 30 (Figures 1a and 1b). Through fitting the coronagraph images of the CME with the GCS

Table 1
The Graduated Cylindrical Shell Modeling Parameters of the Two Coronal Mass Ejections of Interest^a

| No. | Date | ϕ | λ | γ | δ | κ | v (km/s) |
|-----|-----------------|--------|-----------|----------|----------|----------|------------|
| 1 | 2022 January 30 | 34°E | 7°S | 34° | 38° | 0.7 | 777 |
| 2 | 2022 January 31 | 25°W | 12°N | 17° | 11° | 0.4 | 420 |

^a ϕ and λ represent the longitude and latitude of the CME front leading edge in Heliocentric Earth Equatorial (HEEQ) coordinates. They give the propagation direction of the CME. γ and δ are the tilt angle and half-angle of the flux-rope axis, while κ is the sine of the cone half-angle at the flux-rope foot. They are geometric parameters of GCS modeling (Thernisien et al., 2006, 2011). The front velocity (v) is derived from linear-fitting of the CME front leading edge height at different times.

model (Figures 1e and 1f, see Methods for details), we derive that the CME propagated toward 34°E, 7°S in the Heliocentric Earth Equatorial (HEEQ) coordinates with a velocity of about 777 km/s.

This CME passed the Earth with a speed of about 500 km/s during 2nd February 23:03 UT–3rd February 10:53 UT, when Wind spacecraft clearly recorded the signatures of a magnetic cloud, including a strong magnetic field with a smooth rotation, a low proton number density, and a low plasma beta value (the first shaded region in Figure 2). The magnetic cloud provided a nearly 10-hr interval of southward magnetic field with a minimum value close to -20 nT, which led to the geomagnetic storm on 3rd February. On the next day of the CME launch, the active region 12936 generated another CME into a similar direction (Figures 1c and 1d). The GCS modeling result (Figures 1g and 1h) indicates that its propagation direction was about 25°W, 12°N and the speed was about 420 km/s. The CME magnetic cloud, followed by the fast solar wind from the coronal hole around the solar equator, crossed

the Earth on 4th February between 02:55 UT and 20:14 UT (the second shaded region in Figure 2). It consists of two long-lasting intervals of southward magnetic field with the minimum value of about -10 nT, causing another moderate geomagnetic storm with two notable peaks on the same day.

Using the observed solar wind and IMF variations as input, the global upper atmosphere model TIEGCM (described in detail in the Methods section) provides self-consistent simulations of the ionosphere and thermosphere system for understanding the space weather event. During the storm main phase when the IMF turned southward, mass, momentum and energy transfer between the solar wind and magnetosphere is enabled through the magnetic reconnection process (e.g., Akasofu, 1981; Dungey, 1961; Gonzalez et al., 1994). A large amount of electromagnetic energy heated the upper atmosphere via Joule and Ohmic dissipation processes at ionospheric altitudes (e.g., Brekke & Kamide, 1996; McHarg et al., 2005; Thayer et al., 1995), resulting in an expansion of the upper atmosphere which exerts more atmospheric drag when satellites pass through these space-weather active regions (Knipp et al., 2004; Wilson et al., 2006). Figure 3a shows the time variations of the global Joule heating (JH) power. Note that Figure S1 in Supporting Information S1 validates that Joule heating generally converges between different TIEGCM spatial resolutions ($2.5^\circ \times 2.5^\circ$, $1.25^\circ \times 1.25^\circ$, and $0.625^\circ \times 0.625^\circ$). These JH enhancements were well associated with each southward turning of IMF B_z as shown in Figure 3b. The global JH

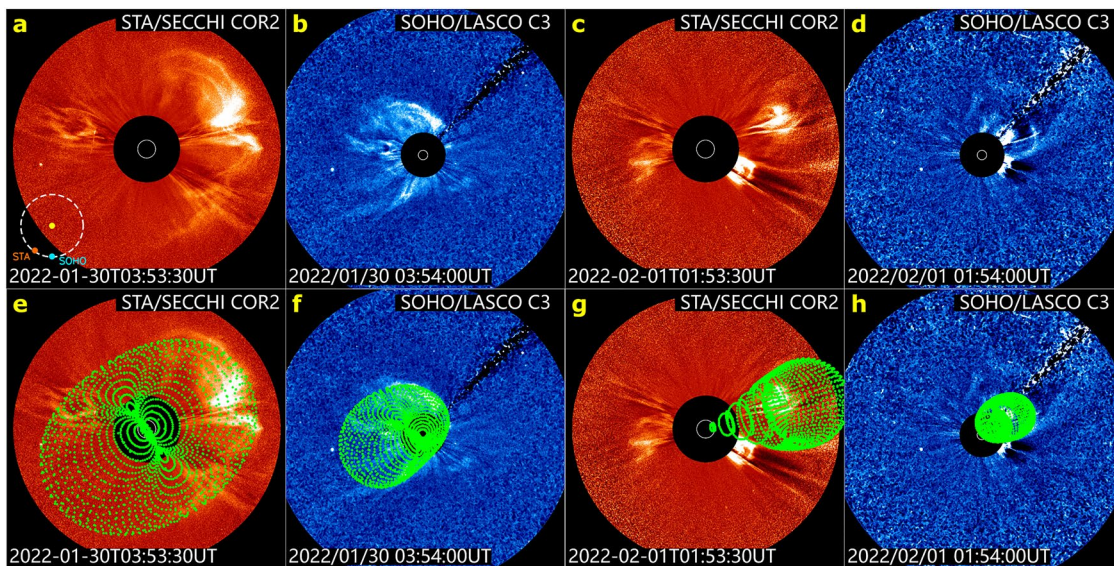


Figure 1. Two Earth-directed coronal mass ejections (CMEs) observed by coronagraphs. (a and b) The difference images of the first CME observed by STA/COR2 and Solar and Heliospheric Observatory/Large Angle and Spectrometric Coronagraph SOHO/LASCO-C3 on 30 January. (c and d) The difference images of the second CME observed by the same coronagraphs on 01 February. (e–h) The same images of (a–d) with the meshes of the Graduated Cylindrical Shell model overlaid. The inset in the lower-left corner of a shows the positions of the SOHO and STA spacecraft.

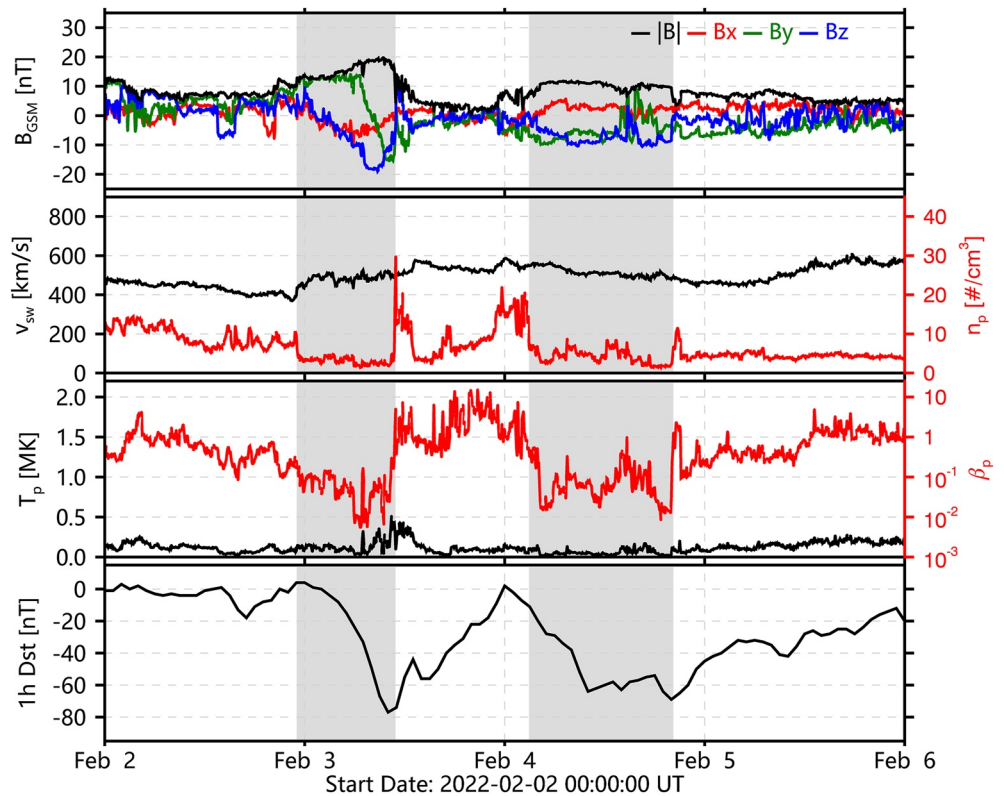


Figure 2. Solar wind and interplanetary magnetic field conditions near the Earth measured by the Wind spacecraft and the Dst index. From top to bottom, the panels show the magnetic field magnitude and components in GSM coordinates, solar wind velocity and proton number density, proton temperature and value of plasma beta, and the Dst index. Two magnetic clouds are indicated by the shadow regions.

power exhibited very dynamic time variations. It reached a maximum of 1040 GW at 08:00 UT during the 3rd February storm, as compared to the typical value of Joule heating power of 95 GW (Knipp et al., 2004). On 4th February there were two smaller JH peaks at 09:00 UT and 17:00 UT. The JH increase was relaxed rapidly after the IMF turned back, while the effects on upper atmosphere would take a longer time to recover. The plot on the schematic Earth in Figure 3c gives the JH during the main phase of the 4th February geomagnetic storm (also see Movie S1 for dynamic temporal variations). Significant JH over 20 erg/cm²/s originated from the electromagnetic energy input can be seen in the noon, dusk, and nightside sectors.

Influenced by the energy deposition into the atmosphere from the solar wind and magnetosphere, Figures 4a–4c display three snapshots of the simulated percentage difference of atmospheric density at 18:00 UT on 3rd February, 03:00 UT on 4th February and 10:00 UT on 4th February with respect to the corresponding UT on 2nd February. At 18:00 UT around the launch time of Starlink satellites (Figure 4a), the geomagnetic storm enhanced the global atmospheric density in a global scale, with most of the enhancements over 12%. Meanwhile, distinct region distributions can be seen, with density perturbations at middle and high latitude much higher than those at low latitude, possibly due to the direct energy deposition from the magnetosphere. The maximum of over 50% percentage was centered at the south pole around 120°E, 80°S. The atmospheric density was then quickly recovered to a relatively quiet amount (Figure 4b and Movie S2), until the subsequent storm occurred. The geomagnetic storm on 4th February caused even larger perturbations in the Earth's upper atmosphere, based on the preconditioning influence of the 3rd February storm. At 10:00 UT, when the IMF B_z was southward, the thermospheric density displayed a global enhancement of over 20% (Figure 4c). The regional density enhancement, for example, the southern polar region, could be larger than 60%. Note that the maximum inclination angle of these Starlink satellites is around 53.2°, suggesting that the satellites mainly experience the atmospheric drag at middle and low latitudes. The first geomagnetic storm was expected by SpaceX as it launched the Starlink satellites at 18:15 UT when the storm had been in the recovery phase and almost reached the quiet level. It seems

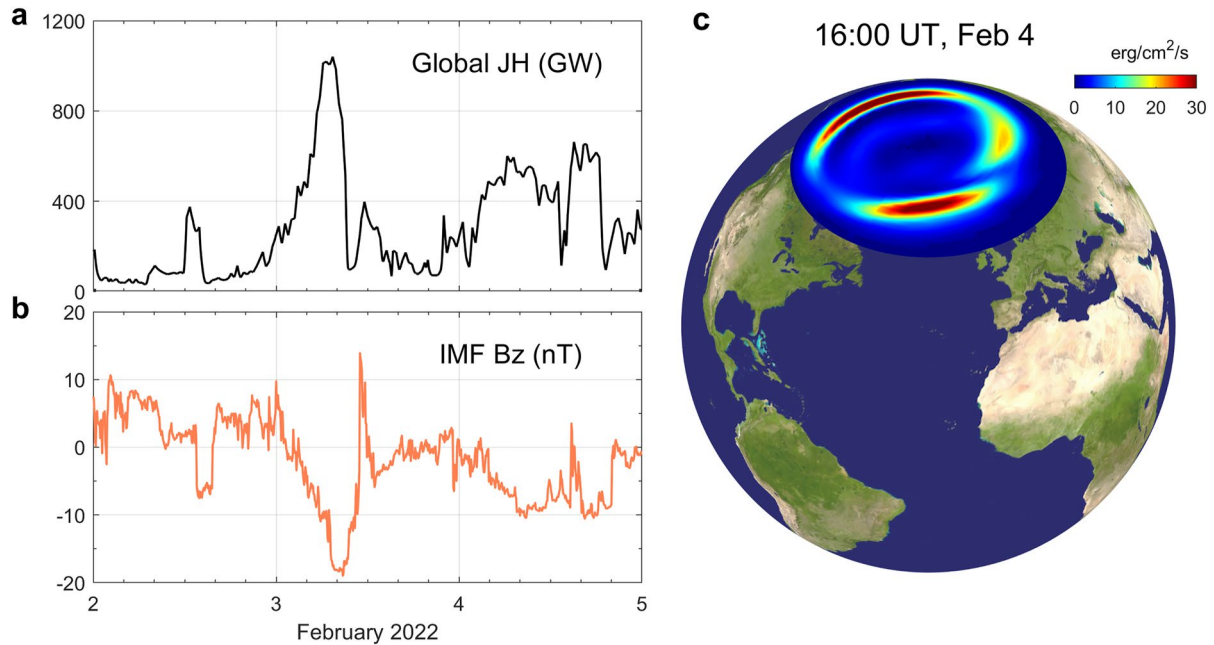


Figure 3. Overview of the energy deposition into the Earth's upper atmosphere. (a and b), The temporal variations of the global power of Joule heating (JH) and the B_z component of interplanetary magnetic field (IMF) during 2–4 February 2022. (c), Snapshot of the polar distribution of height-integrated Joule heating at 16:00 UT on 4th February 2022. The local noon at this UT is around 60°W . The JH was calculated from Thermosphere Ionosphere Electroynamics General Circulation Model based on the equation $Q = \Sigma_P E^2$, where Σ_P represents the height-integrated Pedersen conductivity and E is the electric field. The JH was summed globally by multiplying the surface area of each grid to represent the global JH power. Here the effects of neutral wind on JH are neglected. See Movie S1 for the time variations.

however that the second geomagnetic storm was not predicted which caused the satellites experiencing longer unexpected atmospheric drag.

Figure 4d shows the comparison of atmospheric density from Swarm C observations and TIEGCM simulations during 2–4 February 2022. During this event, Swarm C operated at 9.3 and 21.3 local times with an altitude of approximately 438 km. The observed density increased prominently during 3–4 February, with two peaks of $1.5 \times 10^{-12} \text{ kg/m}^3$ at 12 UT on 3rd February and $1.75 \times 10^{-12} \text{ kg/m}^3$ at 12 UT on 4th February, respectively. The relative enhancement of atmospheric density reached 50% and 75% for the 2 days. As seen by the red lines, the TIEGCM generally reproduced the trend of the observed values at both daytime and nighttime, with similar relative variations during 3–4 February compared to the quiet values on 2 February. We can also note that the TIEGCM has a systematic overestimation of neutral density, which might be associated with the uncertainties of the empirical driving from the magnetosphere as well as from the forcings from the lower atmosphere.

We show the simulated percentage difference of global mean atmospheric density, which is averaged in terms of area, at different altitudes in Figure 4e. Compared to 2nd February, the atmospheric density greatly increased and reached maximum at 12 UT on 3rd February, with global percentage differences of 10%, 21%, 31% and 42% at 150 km, 210 km, 300 km and 400 km, respectively. Particularly, the second moderate storm occurring on 4th February (Figure 2) made the slightly recovered thermosphere enhance to a higher state again. The atmospheric density had two peaks at 12 UT and 18 UT on 4th February, associated with the two southward turnings of IMF B_z in Figure 2. The global density enhancement can be 23% at 210 km and was greater at higher altitudes.

As the satellites were continuously decayed to lower orbits, the accumulative atmospheric drag became increasingly crucial. We have also estimated the decay time of Starlink satellites during storm and quiet time in Figure 4f. The calculation is mainly based on the orbital perturbation equation via the mechanical energy decay of the satellite (Vallado, 2001). Considering only the central gravitational force and atmospheric drag, the mechanical energy decreases under the effect of atmospheric drag. Therefore, during one revolution, the altitude change Δa could be approximately calculated:

$$\Delta a = -\frac{1}{2} \frac{C_D A}{g m_{sat}} \rho v^3 T \quad (1)$$

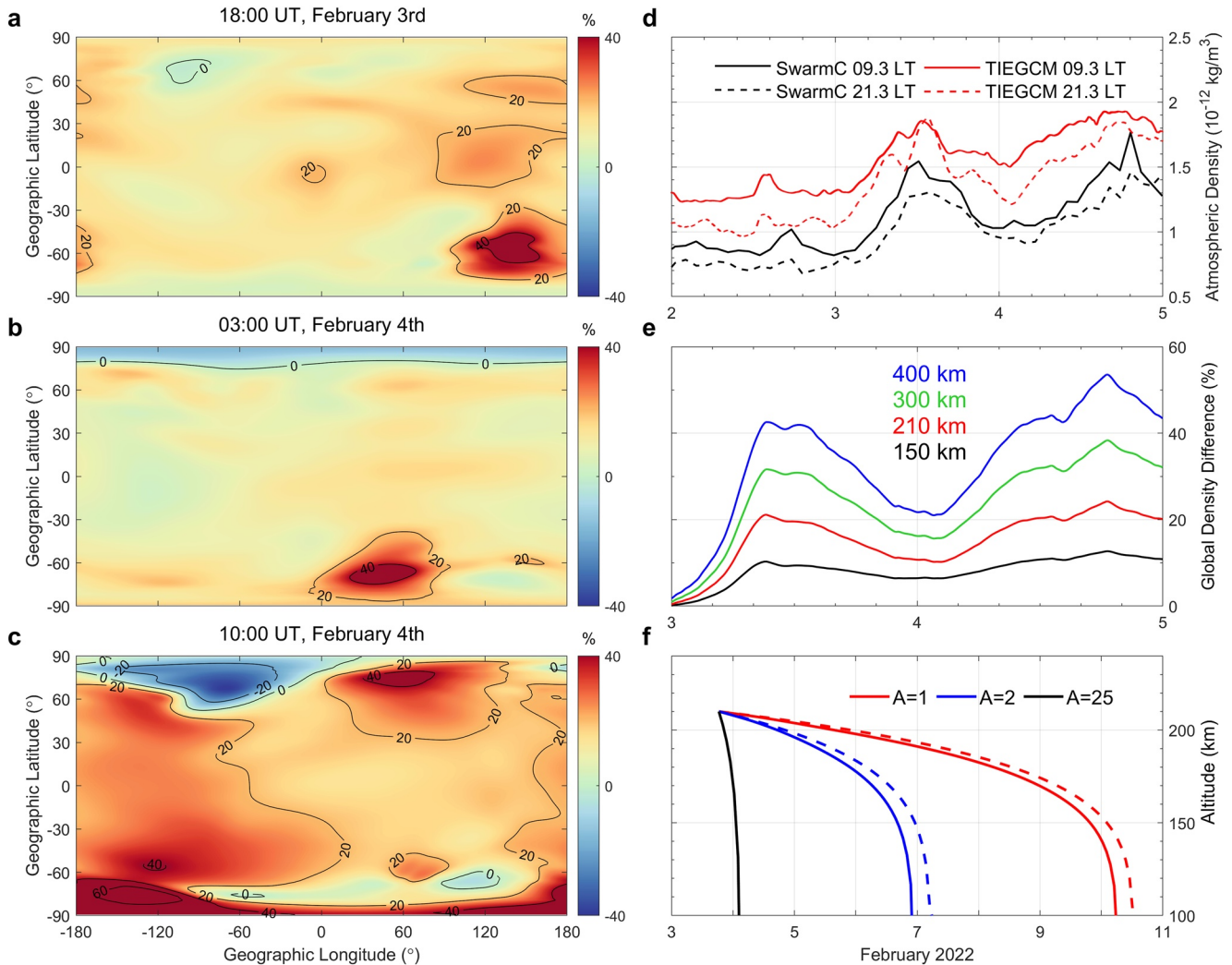


Figure 4. Global atmospheric density disturbance and the orbit decay estimation by the geomagnetic storms. (a–c), Global distribution of the percentage difference of the simulated atmospheric density at 210 km for 18:00 UT on 3rd February (top), 03:00 UT on 4th February (middle) and 10:00 UT on 4th February (bottom) with the reference of the corresponding UT on 2nd February. See Movie S2 for the time variations. (d), The atmospheric density observed by the Swarm-C satellite (black lines) and simulated by Thermosphere Ionosphere Electrodynamics General Circulation Model (TIEGCM) (dashed lines) from 2 to 4th February, 2022 at altitude of around 438 km. (e), The percentage difference of globally averaged atmospheric density from TIEGCM simulations during 3rd and 4th February, 2022 at altitudes of 150 km, 210 km, 300 km, and 400 km. (f), Estimated satellite decay time under cross-section areas of 1 m² (red), 2 m² (blue) and 25 m² (black), with (solid line) and without (dashed line) geomagnetic storm considered.

where g is the gravitational acceleration on the satellite, m_{sat} is the mass of the satellite, C_D is the satellite drag coefficient, A is the cross-section area, ρ stands for the orbital mean density, and T represents the orbit period. We assumed a maximum cross-section area of 25 m² of a satellite when its solar panel is fully deployed and a minimum of 1–2 m². As shown by the black solid line in Figure 4f, in the maximum cross-section area condition, the satellite will fall onto the Earth in less than 1 day in this storm case. Considering the minimum condition, the lifetime of the satellite could be 3–7 days. It is expected that the storm could lead to an enhancement of the thermospheric mass density and the orbital decay rate. The difference in lifetime between storm and quiet time is about 0.5 days. Here we only concentrated on the orbital decay and did not included the predominant conditions. The 0.5-day difference is with respect to the 1–2 m² case.

4. Discussion and Conclusion

The Starlink satellites were initially launched into a low orbit altitude of 210 km, for the purpose that the incorrectly working satellites could be quickly destroyed in the atmospheric drag, rather than becoming space debris. As expected, these satellites will be raised up to the 500 km operational altitude by the ion thruster. The low altitude of 210 km makes satellites experience significant atmospheric drag, especially during the space weather disturbances. From our results, the atmospheric density increased by 23% globally as compared to the quiet condition on 2nd February, and could reach the reported 50% atmospheric drag (from <https://www.spacex.com/updates/>) if considering the orbit decay to a denser low altitude atmosphere.

In this work, we provide a comprehensive review on the process of space weather during this event from the Sun all the way to the terrestrial atmosphere. Two CMEs led to complex geomagnetic activity during 3rd and 4th February, including two sequential storms, albeit with only G1 intensity. This event illustrates the complexity and difficulty of the space weather prediction, and also indicates that even small storms might induce severe astronautical and financial consequences. The solar activity was very quiet for the last 3 years. However, since 2021, the solar activity was starting to ramp up to the next solar maximum in solar cycle 25, and increased geomagnetic activity and space weather events are expected (Hapgood et al., 2022; Owens et al., 2021). Koskinen et al. (2017) listed three influence pathways on Earth's space environment by the Sun: the direct electromagnetic radiation, the interaction of magnetized plasma as discussed by CMEs in this work, and high-energy particles, all of which could significantly impact the satellites and other space weather applications (Knipp et al., 2016; Malandraki & Crosby, 2018; Mewaldt, 2006; Sato et al., 2019). The importance of space weather has become a growing concern, and hence calls for accurate modeling and understanding of the space weather as well as collaborations between industry and space weather community. Note that after this event, the SpaceX team had launched the next series of Starlink satellites to a higher altitude of 300 km to evade the intense drag (Hapgood et al., 2022).

Acknowledgments

This work was supported by the National Natural Science Foundation of China (41974181, 42188101), the B-type Strategic Priority Program of the Chinese Academy of Sciences (XDB41000000), the Project of Stable Support for Youth Team in Basic Research Field, CAS (YSBR-018), the pre-research project on Civil Aerospace Technologies No. D020105 funded by China's National Space Administration, and the Open Research Project of Large Research Infrastructures of CAS—"Study on the interaction between low/mid-latitude atmosphere and ionosphere based on the Chinese Meridian Project". Dang T. was supported by the National Natural Science Foundation of China (42174198, 41904138), the National Postdoctoral Program for Innovative Talents (BX20180286), the China Postdoctoral Science Foundation (2018M642525) and the Fundamental Research Funds for the Central Universities. B.Z. was supported by the General Research Fund (17300719 and 17308520) and the Excellent Young Scientists Fund (Hong Kong and Macau) of the National Natural Science Foundation of China (41922060). Y.W. is particularly grateful to the support of the Tencent Foundation. The authors are grateful for support from the ISSI/ISSI-BJ workshop "Multi-Scale Magnetosphere-Ionosphere-Thermosphere Interaction". This material is based upon work supported by the National Center for Atmospheric Research, which is a major facility sponsored by the National Science Foundation under Cooperative Agreement No. 1852977. The calculations were completed on the supercomputing system in the Supercomputing Center of University of Science and Technology of China.

Conflict of Interest

The authors declare no conflicts of interest relevant to this study.

Data Availability Statement

The STEREO/SECCHI data are produced by a consortium of NRL (USA), RAL (UK), LMSAL (USA), GSFC (USA), MPS (Germany), CSL (Belgium), IOTA (France), and IAS (France) and obtained from STEREO Science Center website (<https://stereo-ssc.nascom.nasa.gov/>). The SOHO/LASCO data are produced by a consortium of the Naval Research Laboratory (USA), Max-Planck-Institut für Aeronomie (Germany), Laboratoire d'Astronomie (France), and the University of Birmingham (UK) and obtained from SOLAR and Heliospheric Observatory website (<https://soho.nascom.nasa.gov/>). The Wind in-situ observation data and Dst index data are available at the Space Physics Data Facility website (<https://cdaweb.gsfc.nasa.gov/>). The high-resolution TIEGCM model is available at <https://github.com/dangt-ustc/TIEGCM2.1>. The observed neutral density is derived from Swarm-C accelerometer data released by ESA (<https://earth.esa.int/eogateway/missions/swarm/data>). The simulation data used in the analyses in this paper are available at website (NSSDC Space Science Article Data Repository: <https://dx.doi.org/10.12176/01.99.02610>). We acknowledge the use of the above data.

References

- Akasofu, S. I. (1981). Energy coupling between the solar wind and the magnetosphere. *Space Science Reviews*, 28(2), 121–190. <https://doi.org/10.1007/BF00218810>
- Anthea, C., Philip, E., Louis, L., Yongliang, Z., & Larry, P. (2021). *Space weather effects and applications*, Wiley.
- Brekke, A., & Kamide, Y. (1996). On the relationship between Joule and frictional heating in the polar ionosphere. *Journal of Atmospheric and Terrestrial Physics*, 58(1), 139–143. [https://doi.org/10.1016/0021-9169\(95\)00025-9](https://doi.org/10.1016/0021-9169(95)00025-9)
- Brueckner, G. E., Howard, R. A., Koomen, M. J., Korendyke, C. M., Michels, D. J., Moses, J. D., et al. (1995). The large angle spectroscopic coronagraph (LASCO). In B. Fleck, V. Domingo, & A. Poland (Eds.), *The SOHO mission* (pp. 357–402). Springer Netherlands. https://doi.org/10.1007/978-94-009-0191-9_10
- Chen, G.-m., Xu, J., Wang, W., & Burns, A. G. (2014). A comparison of the effects of CIR- and CME-induced geomagnetic activity on thermospheric densities and spacecraft orbits: Statistical studies. *Journal of Geophysical Research: Space Physics*, 119(9), 7928–7939. <https://doi.org/10.1002/2014JA019831>
- Chen, G.-m., Xu, J., Wang, W., Lei, J., & Burns, A. G. (2012). A comparison of the effects of CIR- and CME-induced geomagnetic activity on thermospheric densities and spacecraft orbits: Case studies. *Journal of Geophysical Research*, 117(A8). <https://doi.org/10.1029/2012JA017782>

- Dang, T., Zhang, B., Lei, J., Wang, W., Burns, A., Liu, H., et al. (2021). Azimuthal averaging–reconstruction filtering techniques for finite-difference general circulation models in spherical geometry. *Geoscientific Model Development*, 14(2), 859–873. <https://doi.org/10.5194/gmd-14-859-2021>
- Doornbos, E. (2012). *Thermospheric density and wind determination from satellite dynamics*, Springer Science & Business Media. <https://doi.org/10.1007/978-3-642-25129-0>
- Dungey, J. W. (1961). Interplanetary magnetic field and the auroral zones. *Physical Review Letters*, 6(2), 47–48. <https://doi.org/10.1103/PhysRevLett.6.47>
- Emmert, J. T. (2015). Thermospheric mass density: A review. *Advances in Space Research*, 56(5), 773–824. <https://doi.org/10.1016/j.asr.2015.05.038>
- Gonzalez, W. D., Joselyn, J. A., Kamide, Y., Kroehl, H. W., Rostoker, G., Tsurutani, B. T., & Vasyliunas, V. M. (1994). What is a geomagnetic storm? *Journal of Geophysical Research*, 99(A4), 5771–5792. <https://doi.org/10.1029/93JA02867>
- Hapgood, M., Liu, H., & Lugaz, N. (2022). SpaceX—Sailing close to the space weather? *Space Weather*, 20(3), e2022SW003074. <https://doi.org/10.1029/2022SW003074>
- Howard, R. A., Moses, J. D., Vourlidas, A., Newmark, J. S., Socker, D. G., Plunkett, S. P., et al. (2008). Sun Earth connection coronal and heliospheric investigation (SECCHI). *Space Science Reviews*, 136(1), 67. <https://doi.org/10.1007/s11214-008-9341-4>
- Jacchia, L. G. (1959). Two atmospheric effects in the orbital acceleration of artificial satellites. *Nature*, 183(4660), 526–527. <https://doi.org/10.1038/183526a0>
- Knipp, D., Tobiska, W. K., & Emery, B. (2004). Direct and indirect thermospheric heating sources for solar cycles 21–23. *Solar Physics*, 224(1–2), 495–505. <https://doi.org/10.1007/s11207-005-6393-4>
- Knipp, D. J., Ramsay, A. C., Beard, E. D., Boright, A. L., Cade, W. B., Hewins, I. M., et al. (2016). The May 1967 great storm and radio disruption event: Extreme space weather and extraordinary responses. *Space Weather*, 14(9), 614–633. <https://doi.org/10.1002/2016SW001423>
- Koskinen, H. E. J., Baker, D. N., Balogh, A., Gombosi, T., Veronig, A., & von Steiger, R. (2017). Achievements and challenges in the science of space weather. *Space Science Reviews*, 212(3), 1137–1157. <https://doi.org/10.1007/s11214-017-0390-4>
- Krauss, S., Behzadpour, S., Temmer, M., & Lhotka, C. (2020). Exploring thermospheric variations triggered by severe geomagnetic storm on 26 August 2018 using GRACE follow-on data. *Journal of Geophysical Research: Space Physics*, 125(5), e2019JA027731. <https://doi.org/10.1029/2019JA027731>
- Li, R., & Lei, J. (2021a). The determination of satellite orbital decay from POD data during geomagnetic storms. *Space Weather*, 19(4), e2020SW002664. <https://doi.org/10.1029/2020SW002664>
- Li, R., & Lei, J. (2021b). Responses of thermospheric mass densities to the October 2016 and September 2017 geomagnetic storms revealed from multiple satellite observations. *Journal of Geophysical Research: Space Physics*, 126(1), e2020JA028534. <https://doi.org/10.1029/2020JA028534>
- Malandraki, O. E., & Crosby, N. B. (2018). Solar energetic particles and space weather: Science and applications. In O. E. Malandraki & N. B. Crosby (Eds.), *Solar particle radiation storms forecasting and analysis: The HESPERIA HORIZON 2020 project and beyond* (pp. 1–26). Springer International Publishing. https://doi.org/10.1007/978-3-319-60051-2_1
- McHarg, M., Chun, F., Knipp, D., Lu, G., Emery, B., & Ridley, A. (2005). High-latitude Joule heating response to IMF inputs. *Journal of Geophysical Research*, 110(A8), A08309. <https://doi.org/10.1029/2004JA010949>
- McNamara, L. F. (1991). *The ionosphere: Communications, surveillance, and direction finding*, Krieger publishing company.
- Mewaldt, R. A. (2006). Solar energetic particle composition, energy spectra, and space weather. *Space Science Reviews*, 124(1), 303–316. <https://doi.org/10.1007/s11214-006-9091-0>
- Montenbruck, O., & Gill, E. (2000). *Satellite orbits: Models, methods, and applications*, Springer Berlin Heidelberg.
- Owens, M. J., Lockwood, M., Barnard, L. A., Scott, C. J., Haines, C., & Macneil, A. (2021). Extreme space-weather events and the solar cycle. *Solar Physics*, 296(5), 82. <https://doi.org/10.1007/s11207-021-01831-3>
- Pröls, G. W. (2011). Density perturbations in the upper atmosphere caused by the dissipation of solar wind energy. *Surveys in Geophysics*, 32(2), 101–195. <https://doi.org/10.1007/s10712-010-9104-0>
- Qian, L., & Solomon, S. C. (2012). Thermospheric density: An Overview of temporal and spatial variations. *Space Science Reviews*, 168(1), 147–173. <https://doi.org/10.1007/s11214-011-9810-z>
- Richmond, A. D. (1995). Ionospheric electrodynamics using magnetic apex coordinates. *Journal of Geomagnetism and Geoelectricity*, 47(2), 191–212. <https://doi.org/10.5636/jgg.47.191>
- Richmond, A. D., Ridley, E. C., & Roble, R. G. (1992). A thermosphere/ionosphere general circulation model with coupled electrodynamics. *Geophysical Research Letters*, 19(6), 601–604. <https://doi.org/10.1029/92GL00401>
- Roble, R. G., Ridley, E. C., Richmond, A. D., & Dickinson, R. E. (1988). A coupled thermosphere/ionosphere general circulation model. *Geophysical Research Letters*, 15(12), 1325–1328. <https://doi.org/10.1029/GL015i012p01325>
- Sato, H., Jakowski, N., Berdermann, J., Jiricka, K., Heßelbarth, A., Banyś, D., & Wilken, V. (2019). Solar radio burst events on 6 september 2017 and its impact on GNSS signal frequencies. *Space Weather*, 17(6), 816–826. <https://doi.org/10.1029/2019SW002198>
- Skone, S., & Yousuf, R. (2007). Performance of satellite-based navigation for marine users during ionospheric disturbances. *Space Weather*, 5(1). <https://doi.org/10.1029/2006SW000246>
- Thayer, J. P., Vickrey, J. F., Heelis, R. A., & Gary, J. B. (1995). Interpretation and modeling of the high-latitude electromagnetic energy flux. *Journal of Geophysical Research*, 100(A10), 19715–19728. <https://doi.org/10.1029/95ja011159>
- Thernisien, A. (2011). Implementation of the graduated cylindrical shell model for the three-dimensional reconstruction of coronal mass ejections. *The Astrophysical Journal—Supplement Series*, 194(2), 33. <https://doi.org/10.1088/0067-0049/194/2/33>
- Thernisien, A. F. R., Howard, R. A., & Vourlidas, A. (2006). Modeling of flux rope coronal mass ejections. *The Astrophysical Journal*, 652(1), 763–773. <https://doi.org/10.1086/508254>
- Vallado, D. A. (2001). *Fundamentals of astrodynamics and applications* (Vol. 12). Springer Science & Business Media.
- Weimer, D. (2005). Improved ionospheric electrodynamic models and application to calculating Joule heating rates. *Journal of Geophysical Research*, 110(A5), A05306. <https://doi.org/10.1029/2004JA010884>
- Wilson, G. R., Weimer, D. R., Wise, J. O., & Marcos, F. A. (2006). Response of the thermosphere to Joule heating and particle precipitation. *Journal of Geophysical Research*, 111(A10), A10314. <https://doi.org/10.1029/2005ja011274>
- Zhang, K., Li, X., Xiong, C., Meng, X., Li, X., Yuan, Y., & Zhang, X. (2019). The influence of geomagnetic storm of 7–8 september 2017 on the Swarm precise orbit determination. *Journal of Geophysical Research: Space Physics*, 124(8), 6971–6984. <https://doi.org/10.1029/2018JA026316>